Graphical Abstract

Dynamic behavior of droplet transport on realistic gas diffusion layer with inertial effect via a unified lattice Boltzmann method

Jiapei Yang, Linlin Fei, Xiaoqing Zhang, Xiao Ma, Kai H. Luo, Shijin Shuai

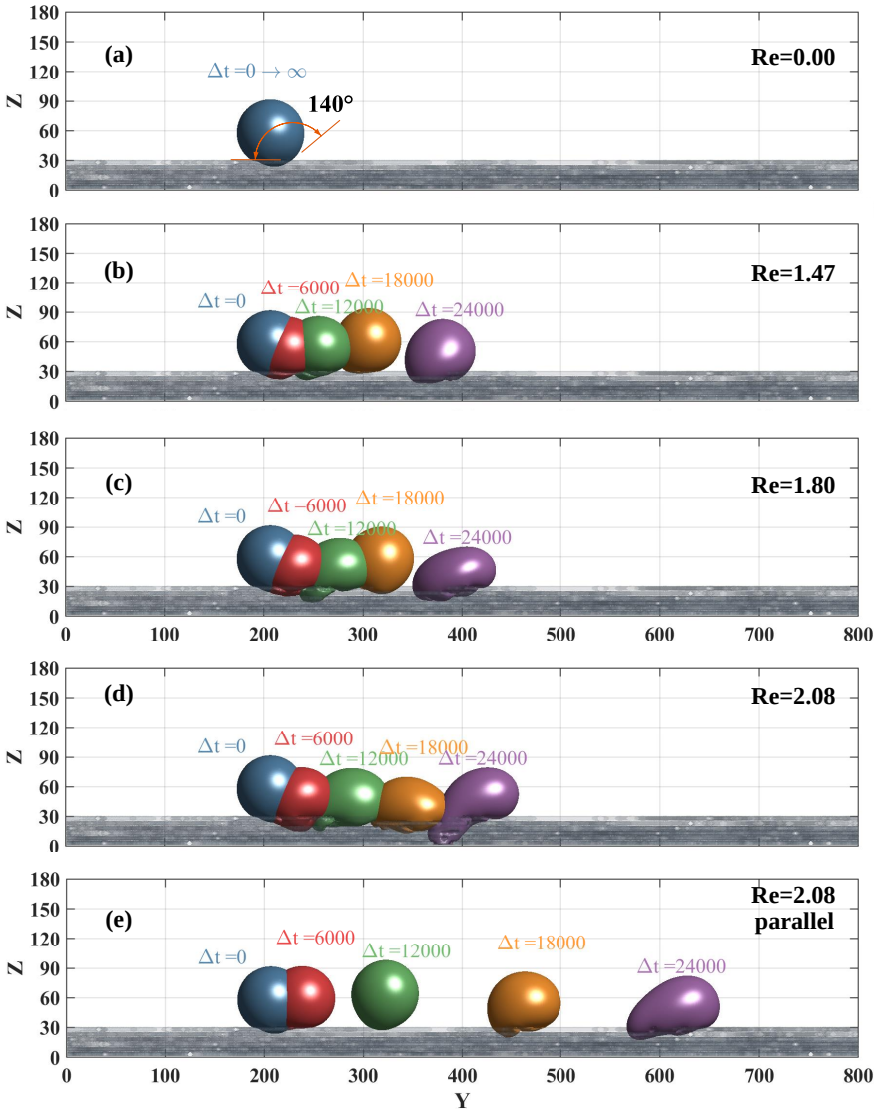

Highlights

Dynamic behavior of droplet transport on realistic gas diffusion layer with inertial effect via a unified lattice Boltzmann method

Jiapei Yang, Linlin Fei, Xiaoqing Zhang, Xiao Ma, Kai H. Luo, Shijin Shuai

- An improved pseudopotential multiphase model within the ULBM framework is adopted.
- The role of inertial effect on droplets on a real GDL surface is revealed.
- The effect of surface wettability on droplet dynamics on the GDL surface is studied.

Dynamic behavior of droplet transport on realistic gas diffusion layer with inertial effect via a unified lattice Boltzmann method

Jiapei Yang[a], Linlin Fei[b], Xiaoqing Zhang[a], Xiao Ma[a,*], Kai H. Luo[c], Shijin Shuai[a]

[a] *State Key Laboratory of Automotive Safety and Energy, School of Vehicle and Mobility, Tsinghua University, Beijing 100084, China*
[b] *Chair of Building Physics, Department of Mechanical and Process Engineering, ETH Zürich (Swiss Federal Institute of Technology in Zürich), Zürich 8092, Switzerland*
[c] *Department of Mechanical Engineering, University College London, Torrington Place, London WC1E 7JE, UK*

Abstract

The dynamic behavior of liquid droplets on a reconstructed real gas diffusion layer (GDL) surface with the inertial effect produced by the three dimensional (3D) flow channel is investigated using an improved pseudopotential multiphase model within the unified lattice Boltzmann model (ULBM) framework, which can realize thermodynamic consistency and tunable surface tension. The microstructure of the GDL (Toray-090) including carbon fibers and polytetrafluoroethylene (PTFE) is reconstructed by a stochastic and mixed-wettability model. The critical force formulation for the Cassie-Wenzel transition of a droplet on GDL surface is derived. The effects of inertia and contact angles on the liquid droplet transport process on a reconstructed real GDL surface with a 3D flow channel are investigated. The results show the normalized center-of-mass coordinate X may enter the channel wall area or fluctuate around the initial position. With increased inertia applied on the droplet, the normalized center-of-mass coordinate Y grows faster and the normalized center-of-mass coordinate Z decreases. It is found by the ULBM for the first time that the liquid droplet is pushed back into the GDL by inertial effect. With the increase of inertia and the decrease of contact angle of GDL, both the droplet penetration depth in GDL and the droplet invasion

fraction increase. The droplet invasion fraction in GDL is up to 30%.

Keywords: Lattice Boltzmann method, Fuel cells, Gas diffusion layer, 3D flow channels, Liquid droplet transport

1. Introduction

The proton exchange membrane fuel cells (PEMFCs) are promising power devices that have high system efficiency, low operating temperature, and zero greenhouse gas emissions, especially for transportation applications [1–3]. Water, as the main product of the electrochemical reaction in the cathode catalyst layer (CL), will accumulate in the gas diffusion layer (GDL) and gas channel (GC) if liquid water was not removed in time, which is well known as "water flooding" [4]. And at the same time, excessive liquid water in GDL and GC blocks the transport passage between reactants and the CL, which reduces the performance of PEMFCs [5–8]. Commonly, GDL has a random and complex geometry structure and consists of a porous substrate (including carbon fiber paper or carbon cloth) treated with a hydrophobing agent [9].

In order to analyse and identify flooding phenomena, numerous experimental and numerical investigations have been conducted into the dynamic behavior of liquid water in GC. Experimental investigations were usually conducted by optical visualization, fluorescence microscopy, neutron imaging, and X-ray radiography [10, 11]. Kumbur et al. [12] used a top-transparent channel with a diffusion media (DM) on the bottom side to replicate the main features of flow channels of the PEMFCs. They observed that the surface wettability of the DM enhanced the removal of liquid droplet at high flow rates. Theodorakakos et al. [13] also investigated the dynamic process through a transparent PEM fuel cell. Fishman et al. [14] obtained the side-view images of droplet on the real GDL material by the fluorescence

*Corresponding author.
Email address: max@tsinghua.edu.cn (Xiao Ma)

microscopy technology. Wu and Djilali [15] proposed a transparent microfluidic platform with a smooth undersurface to represent the cathode GC. They obtained the flow pattern map of liquid water emergence phenomena, which depended on the air and water velocities. The results showed that the flow regime changed from slug to droplet flow as the air velocity increased. Rahimian et al. [16] employed the synchrotron X-ray radiographic imaging technique to observe the through-plane behavior of liquid droplet in GC under various air flow rates. Iranzo et al. [17] carried out the neutron imaging technique to investigate the in-plane evolution of liquid water for an operating fuel cell. However, most experimental studies reported so far provided little information about the space and time evolutions of liquid water behavior due to the limited visual ability of experimental techniques and high cost.

In addition to experimental work, numerical simulations have been conducted to investigate the transport behavior of liquid water in GC. Wang et al. [18] employed molecular dynamics (MD) to simulate the droplet dynamic process on the rough GDL surface and found that the contact angle of droplet was dominated by the roughness. Using the volume of fluid (VOF) method, Zhu et al. [19] studied the dynamical behavior of liquid water that entered the channel of fuel cell through a GDL pore. They assumed that the GDL surface was flat rather than rough. Chen et al. [20] numerically investigated the influences of the surface structure of the GDL on the transport behavior of a liquid droplet in the GC via the VOF method. The real microstructure of GDL surface was replaced by some regular geometries for the sake of simplification. Ashrafi and Shams [21] used the 2D VOF method to investigate the movement process of liquid droplet on the GDL surface generated by a random function. Anyanwu et al. [22] used a reconstructed GDL as the bottom of GC to study the droplet behavior on GDL through the VOF model. They found that the GDL structure influenced the droplet dynamics. The rough GDL surface was generated by Gaussian height distribution function and autocovariance function to studied the influence of

GDL roughness on the water removal using a 2D VOF method [23]. Their results showed that the GDL surface with higher roughness can drain water droplet more efficiently in the GC. In addition, the VOF method has been adopted to capture the water transport process inside the GC [24–26].

Recently, the lattice Boltzmann (LB) method has been become a popular method for two-phase flow simulations, especially in complex geometry [27–32]. Hao and Cheng [33] proposed a multiphase free-energy LB method to present the water droplet behavior including formation and removal in the GC, which was a flat surface rather than the actual GDL surface. They found that the higher the contact angle of GDL surface is, the higher altitude the droplet was lifted from the surface, which brought about more reactant transport pathway in the GDL surface. Amara and Nasrallah [34] used the pseudopotential LB model to explore the droplet behavior of droplet on the flat surface in the micro-channel. Xu et al. [35] presented a pseudopotential LB model to simulate the droplet motion in a GC with rough undersurface, which was simplified as many micropillars. Yang et al. [36] introduced the contact angle hysteresis to a droplet moving on the flat surface at large Bond number by the means of the pseudopotential LB model. Hou et al. [37] developed a multi-component pseudopotential LB model to investigate the liquid water droplet movement in the GC with a GDL microstructure. It is revealed that the realistic microstructure could enforce the GDL wettability and the liquid water droplet moved more quickly when the GDL was more hydrophobic.

In the last decade, the three dimensional (3D) flow channels, which are characterised by a convective flow perpendicular to the GDL surface [3], have attracted many researchers to explore in depth [38–43]. And the 3D fine-mesh flow channel, which is a type of 3D flow channels, has been adopted in Toyota MIRAI fuel cell vehicles [44]. Kuo et al. [38, 39] firstly investigated the performance of a wave-like channel (also a type of the 3D flow channels) in fuel cells. Their results indicated that the larger gas flow velocity in GC led to the increase of

the reaction rate in CLs. But the gas flow inside GDL could not be obtained in their study. The multiphase mixture model coupled with Forchheimer's inertial was established by Kim et al. [45] to study the two-phase transport in the GDL with the 3D flow channel. They found that the liquid water transport characteristics would be influenced by the inertial effect towards the GDL surface, which was due to gas flow guided into the GDL by the 3D flow channel. From the above studies, it is also necessary to consider the inertial effect of gas flow towards the GDL surface on the liquid droplet on the real surface of GDL.

To the best of our knowledge, the simulation of liquid droplet behavior on the reconstructed real GDL surface with the inertial force towards the GDL surface at the pore scale has not been reported yet. Therefore, in this study, we simulate the dynamic behavior of liquid droplet by the means of an improved pseudopotential multiphase LB model, which can realize thermodynamic consistency and tunable surface tension. The microstructure of the GDL (Toray-090) including carbon fibers and polytetrafluoroethylene (PTFE) is reconstructed by a stochastic and mixed-wettability model. The effects of inertia and GDL wettability on the liquid droplet transport process on the reconstructed real GDL surface are investigated. The rest of this paper is structured as follows. Section 2 briefly presents the improved pseudopotential multiphase LB model, and then describes the computation domain and system setup. Section 3 shows the numerical results and discussion. The final section is the conclusion.

2. A unified lattice Boltzmann model

According to the scheme of collision process, the LB model can be classified into several categories, such as single-relaxation-time (SRT) [46], multi-relaxation-time (MRT) [47] and non-orthogonal MRT LB model [48, 49], which has recently been put into an unified lattice Boltzmann model (ULBM) framework [50]. The present paper focuses on the non-orthogonal MRT LB model, which simplifies the mapping matrix between the velocity space and moment

space and shows good transportability and great flexibility among the lattice schemes. To simulate multiphase flows, the pseudopotential model is employed in combination of the non-orthogonal MRT LB scheme since it is widely used and has been extensively developed in terms of large density ratio, thermodynamic consistency and tunable surface tension in recent years [29, 30, 36, 49, 51–53]. For a detailed introduction to non-orthogonal MRT LB model and pseudopotential model, please refer to the comprehensive review papers [27, 54] and our previous studies [29, 30, 36, 49, 51–53]. In this section, the D3Q19 non-orthogonal MRT pseudopotential LB model, which has been validated in our previous paper [51], is briefly introduced as follows.

2.1. The non-orthogonal MRT LB model

The LB equation including evolution and collision process within the ULBM framework can be expressed as [50]

$$f_i\left(\mathbf{x}+\mathbf{e}_i\Delta t, t-\Delta t\right)-f_i(\mathbf{x},t)=-\left(\mathbf{N^{-1}M^{-1}SMN}\right)\left[f_i\left(x,t\right)-f_i^{eq}\left(x,t\right)\right]+\mathbf{N^{-1}M^{-1}}(\mathbf{I}-\mathbf{S}/2)\mathbf{MN}\Delta t\bar{F}_i \tag{1}$$

where $f_i(\mathbf{x},t)$ is the particle distribution function at spatial position $\mathbf{x}$ and time t, $\mathbf{e}_i$ is the discrete velocity vector along the direction i, $\Delta t=1$ lattice unit (lu) is the time step, f_i^{eq} is the equilibrium particle distribution function, $\mathbf{I}$ is a unit tensor matrix, $\mathbf{N}$ is set to be $\mathbf{I}$ to make the ULBM reduce to a non-orthogonal MRT scheme. $\mathbf{M}$, $\bar{F}_i$, and $\mathbf{S}$ are non-orthogonal transformation matrix, the discrete forcing term in the non-orthogonal MRT scheme, and

diagonal matrix of relaxation, respectively, given by

$$\mathbf{M} = \begin{bmatrix}
1 & 1 & 1 & 1 & 1 & 1 & 1 & 1 & 1 & 1 & 1 & 1 & 1 & 1 & 1 & 1 & 1 & 1 & 1 \\
0 & 1 & -1 & 0 & 0 & 0 & 0 & 1 & -1 & 1 & -1 & 1 & -1 & 1 & -1 & 0 & 0 & 0 & 0 \\
0 & 0 & 0 & 1 & -1 & 0 & 0 & 1 & 1 & -1 & -1 & 0 & 0 & 0 & 0 & 1 & -1 & 1 & -1 \\
0 & 0 & 0 & 0 & 0 & 1 & -1 & 0 & 0 & 0 & 0 & 1 & 1 & -1 & -1 & 1 & 1 & -1 & -1 \\
0 & 0 & 0 & 0 & 0 & 0 & 0 & 1 & -1 & -1 & 1 & 0 & 0 & 0 & 0 & 0 & 0 & 0 & 0 \\
0 & 0 & 0 & 0 & 0 & 0 & 0 & 0 & 0 & 0 & 0 & 1 & -1 & -1 & 1 & 0 & 0 & 0 & 0 \\
0 & 0 & 0 & 0 & 0 & 0 & 0 & 0 & 0 & 0 & 0 & 0 & 0 & 0 & 0 & 1 & -1 & -1 & 1 \\
0 & 1 & 1 & 1 & 1 & 1 & 1 & 2 & 2 & 2 & 2 & 2 & 2 & 2 & 2 & 2 & 2 & 2 & 2 \\
0 & 1 & 1 & -1 & -1 & 0 & 0 & 0 & 0 & 0 & 0 & 1 & 1 & 1 & 1 & -1 & -1 & -1 & -1 \\
0 & 1 & 1 & 0 & 0 & -1 & -1 & 1 & 1 & 1 & 1 & 0 & 0 & 0 & 0 & -1 & -1 & -1 & -1 \\
0 & 0 & 0 & 0 & 0 & 0 & 0 & 1 & -1 & 1 & -1 & 0 & 0 & 0 & 0 & 0 & 0 & 0 & 0 \\
0 & 0 & 0 & 0 & 0 & 0 & 0 & 0 & 0 & 0 & 0 & 1 & -1 & 1 & -1 & 0 & 0 & 0 & 0 \\
0 & 0 & 0 & 0 & 0 & 0 & 0 & 1 & 1 & -1 & -1 & 0 & 0 & 0 & 0 & 0 & 0 & 0 & 0 \\
0 & 0 & 0 & 0 & 0 & 0 & 0 & 0 & 0 & 0 & 0 & 1 & 1 & -1 & -1 & 0 & 0 & 0 & 0 \\
0 & 0 & 0 & 0 & 0 & 0 & 0 & 0 & 0 & 0 & 0 & 0 & 0 & 0 & 0 & 1 & -1 & 1 & -1 \\
0 & 0 & 0 & 0 & 0 & 0 & 0 & 0 & 0 & 0 & 0 & 0 & 0 & 0 & 0 & 1 & 1 & -1 & -1 \\
0 & 0 & 0 & 0 & 0 & 0 & 0 & 1 & 1 & 1 & 1 & 0 & 0 & 0 & 0 & 0 & 0 & 0 & 0 \\
0 & 0 & 0 & 0 & 0 & 0 & 0 & 0 & 0 & 0 & 0 & 1 & 1 & 1 & 1 & 0 & 0 & 0 & 0 \\
0 & 0 & 0 & 0 & 0 & 0 & 0 & 0 & 0 & 0 & 0 & 0 & 0 & 0 & 0 & 1 & 1 & 1 & 1
\end{bmatrix} \tag{2}$$

$$\bar{F}_i = \omega\left(|\mathbf{e}_i|^2\right)\left[\frac{\mathbf{e}_i - \mathbf{u}}{c_s^2} + \frac{(\mathbf{u}\cdot\mathbf{e}_i)\,\mathbf{e}_i}{c_s^4}\right]\cdot\mathbf{F} \tag{3}$$

$$\mathbf{S} = \mathrm{diag}\left(s_0, s_1, s_1, s_1, s_v, s_v, s_v, s_b, s_v, s_v, s_3, s_3, s_3, s_3, s_3, s_3, s_4, s_4, s_4\right) \tag{4}$$

where ω is weights ($\omega(0) = 1/3$, $\omega(1) = 1/18$ and $\omega(2) = 1/36$), $c_s^2 = 1/3$ is sound speed by the lattice, $\mathbf{u}$ and $\mathbf{F}$ are respectively the velocity and total force of fluid node, $s_v =$

$1/(\nu/c_s^2/\Delta t + 0.5)$ and $s_b = 2/3/(\xi/c_s^2/\Delta t + 0.5)$ are relaxation coefficients respectively related to the kinematic and bulk viscosities. In this paper, $\nu_{\rm l} = 0.01$ and $\nu_{\rm g} = 0.1497$ are respectively adopted for liquid and vapor phases, which is in accordance with the ratio of water to air viscosity at 20 °C.

In the D3Q19 non-orthogonal MRT LBM, the 19 elements of the moment set vector $\mathbf{m} = \mathbf{M}\mathbf{f}$ are as follows [49]

$$\begin{aligned}\mathbf{m} = [&k_{000}, k_{100}, k_{010}, k_{001}, k_{110}, k_{101}, k_{011}, k_{200} + k_{020} + k_{002}, k_{200} - k_{020}, \\ &k_{200} - k_{002}, k_{120}, k_{102}, k_{210}, k_{201}, k_{012}, k_{021}, k_{220}, k_{202}, k_{022}]^{\rm T}\end{aligned} \tag{5}$$

where $k_{mnp} = \left\langle f_i \mid e_{ix}^m e_{iy}^n e_{iz}^p \right\rangle$.

The macroscopic variables can be obtained by

$$\rho = \sum_i f_i, \quad \rho\mathbf{u} = \sum_i f_i e_i + \frac{\Delta t \mathbf{F}}{2} \tag{6}$$

2.2. The pseudopotential multiphase model

The pseudopotential multiphase model originally proposed by Shan and Chen [55, 56] (also called Shan-Chen model), is a widely used multiphase model in the LB community. In this model, the interactions among fluid particles are modeled based on a density-dependent pseudopotential function, i.e.

$$\mathbf{F}_{\rm int} = -G\psi(\mathbf{x})/c_s^2 \sum_i \omega\left(|\mathbf{e}_i|^2\right) \psi\left(\mathbf{x} + \mathbf{e}_i \Delta t\right) \mathbf{e}_i \tag{7}$$

where the pseudopotential scheme $\psi = \sqrt{2\left(p_{\rm EOS} - \rho c_s^2\right)/Gc^2}$ is adopted from [57] and G is set to be -1.0.

In order to enable the multiphase flow simulation to reach good thermodynamic consistency and tunable surface tension, several terms of $\bar{\mathbf{F}}$ in moment space are modified by

[49]

$$
\begin{gathered}
(M\bar{F})'_4 = (M\bar{F})_4 - \frac{Q_{xy}}{\left(s_v^{-1}-0.5\right)\Delta t}, (M\bar{F})'_5 = (M\bar{F})_5 - \frac{Q_{xz}}{\left(s_v^{-1}-0.5\right)\Delta t}, (M\bar{F})'_6 = (M\bar{F})_6 - \frac{Q_{yz}}{\left(s_v^{-1}-0.5\right)\Delta t} \\
(M\bar{F})'_7 = (M\bar{F})_7 + \frac{6\varepsilon|F_{int}|^2}{\psi^2\left(s_e^{-1}-0.5\right)\Delta t} + \frac{4(Q_{xx}+Q_{yy}+Q_{zz})}{5\left(s_e^{-1}-0.5\right)\Delta t} \\
(M\bar{F})'_8 = (M\bar{F})_8 - \frac{(Q_{xx}-Q_{yy})}{\left(s_v^{-1}-0.5\right)\Delta t}, \\
(M\bar{F})'_9 = (M\bar{F})_9 - \frac{(Q_{xx}-Q_{zz})}{\left(s_v^{-1}-0.5\right)\Delta t}
\end{gathered} \tag{8}
$$

where the mechanical stability condition is adjusted by factor ε. The tensor $Q_{\alpha\beta}$ can be obtained from

$$
Q_{\alpha\beta} = \kappa\frac{G}{2}\psi(x)\sum_i w\left(|\mathbf{e}_i|^2\right)\left[\psi\left(\mathbf{x}+\mathbf{e}_i\Delta t\right)-\psi(\mathbf{x})\right]\mathrm{e}_{i\alpha}e_{i\beta} \tag{9}
$$

where the surface tension is tuned by the parameter κ.

In this paper, the wettability of fibers and PTFE in GDL is implemented by the modified pseudopotential-based fluid–solid interaction scheme [58] and weighted average density of ghost fluid nodes close to solid boundary [51], which are given by

$$
\mathbf{F}_{\mathrm{ads}}(\mathbf{x}) = -G_{\mathrm{ads}}\psi(\mathbf{x})\sum_i w\left(|\mathbf{e}_i|^2\right)\psi(\mathbf{x})s\left(\mathbf{x}+\mathbf{e}_i\Delta t\right)\mathbf{e}_i \tag{10}
$$

$$
\rho_{\mathrm{ghost}}(\mathbf{x}) = \frac{\sum_i \omega_i\rho\left(\mathbf{x}+\mathbf{e}_i\Delta t\right)\left(1-s\left(\mathbf{x}+\mathbf{e}_i\Delta t\right)\right)}{\sum_i \omega_i\left(1-s\left(\mathbf{x}+\mathbf{e}_i\Delta t\right)\right)} \tag{11}
$$

where the contact angle is controlled by parameter G_{ads}, and fluid/solid nodes are respectively represented by switching function $s\left(\mathbf{x}+\mathbf{e}_i\Delta t\right) = 0/1$, the weights ω_i is $1/3(i = 0), 1/18(i = 1-6), 1/36(i = 7-18)$.

2.3. Model validation

In order to test whether the surface tension is tunable, the simulation of a droplet in a $200 \times 200 \times 200$ cube with periodic boundary condition is conducted. The radius of the droplet is changed in the range of $R = [30, 35, 40, 45, 50]$ lu. The law of Laplace describes the relationship between the pressure difference ($\Delta p = p_{\text{int}} - p_{\text{out}}$) and the droplet radius by

$$\Delta p = 2\gamma / R \tag{12}$$

where γ is surface tension.

Figure 1 shows the numerical results between pressure difference Δp and $2/R$ at $\kappa = 0.0, 0.15$ and 0.3 by the LB model, which is clearly consistent with the Laplace's law. In addition, it should be noted that the non-orthogonal MRT LB multiphase model has been validated through the theoretical results of liquid water invasion through a perforated plate and the experimental results of capillary pressure P_c—saturation s curves of GDL in our previous research [51].

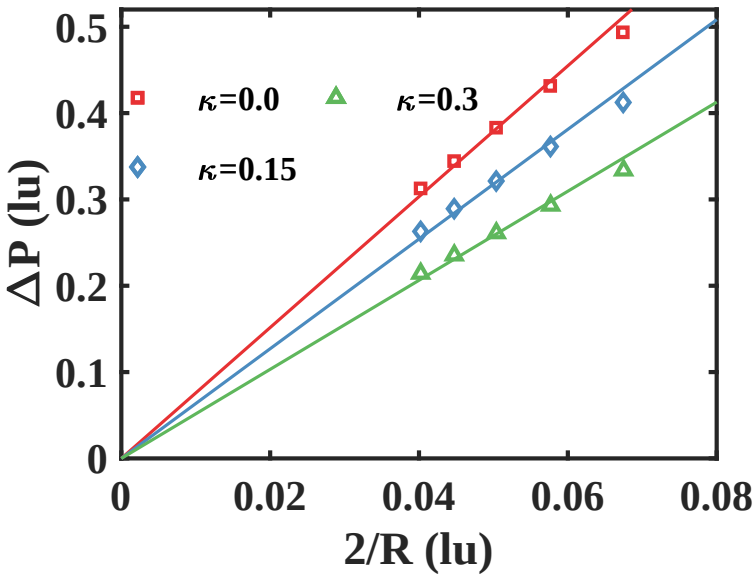

Figure 1: The relationship between pressure difference Δp and $2/R$ at $\kappa = 0.0, 0.15$ and 0.3.

2.4. Critical force formulation

For a liquid water droplet on the top of the rough structure of GDL, the Wenzel state [59] and Cassie state [60] are the two typical forms of water droplets, as shown in Fig. 2. When additional vertical force or pressure is applied to the droplet on the porous GDL surface, a transition from Cassie to Wenzel state can be induced. Zheng et al. [61] proposed the force-balance relation for the Cassie-Wenzel transition of water-gas interface, i.e.

$$p_c A = -\gamma L \cos\theta \tag{13}$$

where p_c is the critical pressure on the water-air interface, A is the difference between the area of total water-air interface and cross sections, L is the perimeter of the cross sections, θ is contact angle.

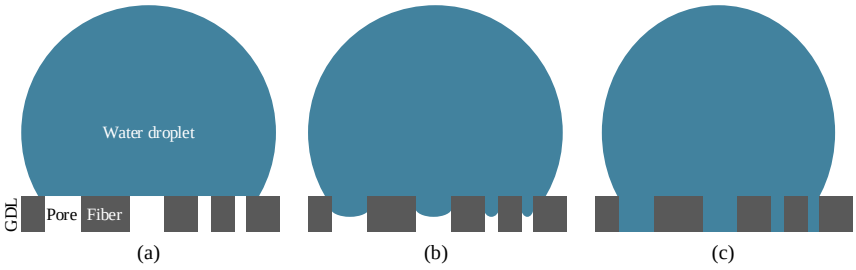

Figure 2: A sketch of wetting states:(a) Cassie state; (b) Cassie-Wenzel transition state; (c)Wenzel state.

In Eq. (13), the left-hand side denotes the total vertical pressure applied to the droplet while the right-hand side denotes the vertical component of the water-air surface tension. Inspired by Eq. (13), the force-balance relation of liquid water droplet on the porous GDL can be obtained as a function of critical body force acting on the droplet, which is given by

$$g_c V \rho \frac{A_{\text{pore}}}{S} = -\gamma L_{\text{pore}} \cos\theta \tag{14}$$

where g_c is the critical body force, ρ is the density of droplet, A_{pore} and L_{pore} are, respectively,

the area and perimeter of the pore, V and S are, respectively, the volume and bottom area of the spherical cap with the contact angle θ and radius R, i.e.

$$V = \frac{\pi}{3}R^3(2+\cos\theta)(1-\cos\theta)^2, S = 2\pi R^2(1-\cos\theta) \tag{15}$$

Thus the critical body force g_c for Cassie-Wenzel transition can be obtained by substituting Eq. (15) into Eq. (14)

$$g_c = -\frac{6\gamma\cos\theta L_{\text{pore}}}{\rho R(2+\cos\theta)(1-\cos\theta)A_{\text{pore}}} \tag{16}$$

2.5. Computation domain and initial conditions

In this paper, the GDL is reconstructed by the means of our previous work [51]. The through-plane porosity distribution of reconstructed GDL agrees well with the experimental result [62]. It is noted that the porosity distribution of Toray-090 (10w% PTFE) close to GDL surface is adopted to reconstruct the GDL in the computation domain for the sake of reducing the computational load, as shown in Fig. 3. This range of porosity distribution consists of the trough and greatest change rate of the whole porosity distribution.

The whole computation domain consists of a GDL ($800 \times 150 \times 30$ lu^3) and a channel ($800 \times 150 \times 150$ lu^3). The GDL is made up of six layers of carbon fiber with the diameter of 5 lu. At the initial time, the center of mass of a droplet with the diameter D of 70 lu is placed at the initial positions $X_0 : 200$ $lu, Y_0 : 75$ $lu, Z_0 : 52$ lu. The periodic boundary condition is applied to the boundary along the flow direction while the non-slip wall boundary condition is implemented at the other boundary.

In this study, we consider the inertial effect introduced by the upstream of 3D flow channel, which means the direction of the inertial effect is towards the interior of the GDL (indicated by the direction of the arrow in Fig. 4). The inertial effect is in the plane along the direction of the channel and the inclination angle is selected to be 45°. In addition, the

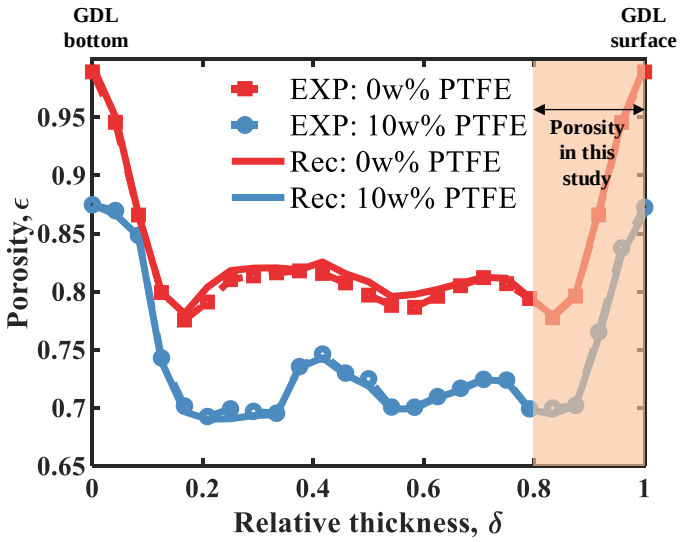

Figure 3: The comparisons of through-plane porosity distribution of reconstructed and experimental [62] Toray-090 GDL (10w% PTFE) and the range of porosity distribution of the GDL adopted in this paper (indicated by the arrow).

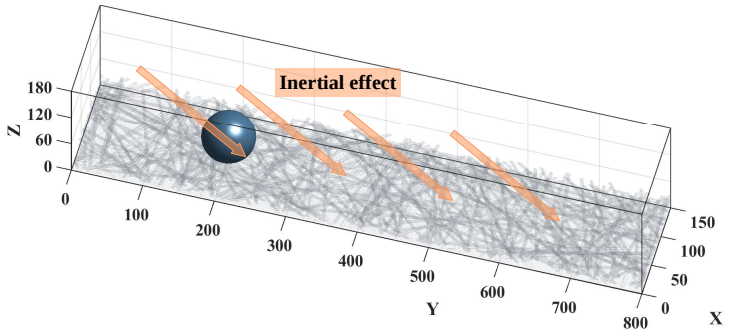

Figure 4: Schematic of computation domain and system setup.

inertial effect that parallels to the GDL surface is adopted as a traditional case. The inertial effect is represented by the body force [54]:

$$\mathbf{F}_{\text{body}} = (\rho - \rho_{\text{g}})\,\mathbf{g}_{\text{b}} \tag{17}$$

where g_{b} is a parameter to adjust the body force and ρ_{g} is the density of air.

In order to nondimensionalize the inertial effect, we can introduce a characteristic length

L_0 and characteristic velocity U_0. Here, L_0 is set to be the fiber diameter (6 lu) and U_0 is given by

$$U_0 = \sqrt{g_b L_0} \tag{18}$$

Then, the dimensionless Reynolds number can be obtained by

$$Re = U_0 L_0 / \nu_l = {g_b}^{1/2} {L_0}^{3/2} / \nu_l \tag{19}$$

Therefore, in this paper, the various inertial effects are investigated at $Re = 0, 1.47, 1.80, 2.08$. It is noted that $Re = 0$ describes the condition without inertial effects, which is a base case.

Figure 5 shows the evolution process of the center of mass position of the spherical-cap droplet on the GDL. It can be seen that the center of mass positions, including X_c, Y_c, and Z_c positions do not remain still at the initial positions X_0, Y_0, Z_0; instead, they fluctuate periodically and gradually become stable. The stable positions are X_s : 72.70 lu, Y_s : 206.80 lu, and Z_s : 57.78 lu at the time of 130000 lu. Hence, in the following sections, the various inertial effects are applied at $t_0 = 130000$ lu and the time Δt starts at time t_0.

3. Results and discussion

In this section, the effects of inertia and contact angles on the liquid droplet transport on the GDL are studied. And the quantitative analysis of liquid droplet morphology is presented.

3.1. Roles of inertial effect

The front-view and axis-view snapshots of the droplet transport process on the GDL surface with various inertial effects are presented in Fig. 6. From the base case ($Re = 0.00$), the contact angle of liquid droplet on the GDL can be obtained and is equal to 140°, as shown in the left hand of Fig. 6(a). By applying various magnitudes of inertial effects on the

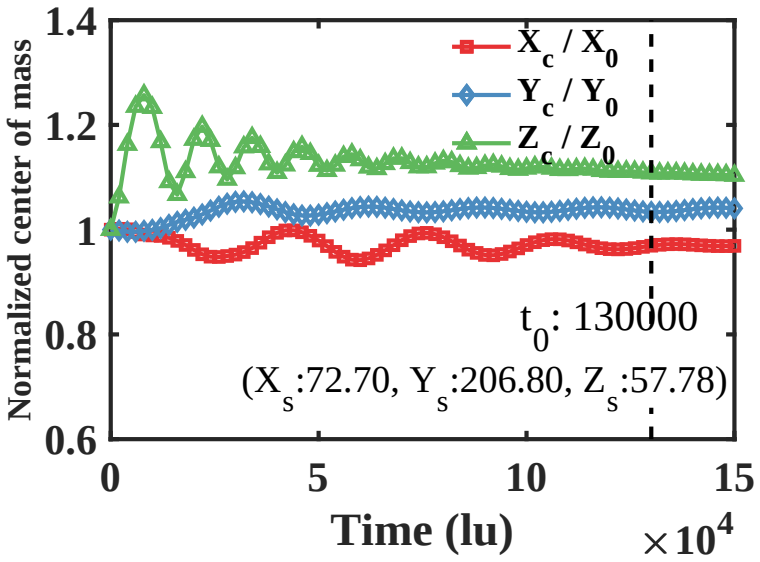

Figure 5: Time evolution process of the center of mass positions of the spherical-cap droplet on the GDL surface. The X_c, Y_c, Z_c positions are respectively normalized by the initial position X_0 : 200 lu, Y_0 : 75 lu, Z_0 : 52 lu. And the mass center positions gradually tend to the stable positions X_s : 72.70 lu, Y_s : 206.80 lu, and Z_s : 57.78 lu at the time of 130000 lu.

liquid droplet, the droplet transport phenomena on the rough GDL are illustrated in Fig. 6. It is found that the liquid droplets periodically move closer and away from the side wall of channel rather than moving forward the outlet along a straight line in a smooth plane [36]. In particular, it is observed that the droplet with $Re = 1.47$ is even reaching the side wall, as shown in Fig. 6(b). It can be explained that the existence of real and random surface of GDL produces a force toward the side wall. In addition, a rare and interesting phenomenon is identified from the front view of droplet transport that the liquid droplet penetrates into the GDL by inertial effect. And the higher the inertial effect is, the more deeply the liquid droplet penetrates into the GDL. When $Re = 2.88$, part of the droplet reaches the bottom of GDL and then droplet breakup occurs, as shown in Fig. 6(d). However, for the case with the same inertial effect parallel to the GDL surface in Fig. 6(e), the droplet is still on the GDL surface except for a small penetration due to the larger size of local pore. It is also found that the droplet in Fig. 6(e) moves faster than in Fig. 6(d). This can be explained that the inertial effects perpendicular to the GDL surface increase the resistance introduced

by the carbon fiber.

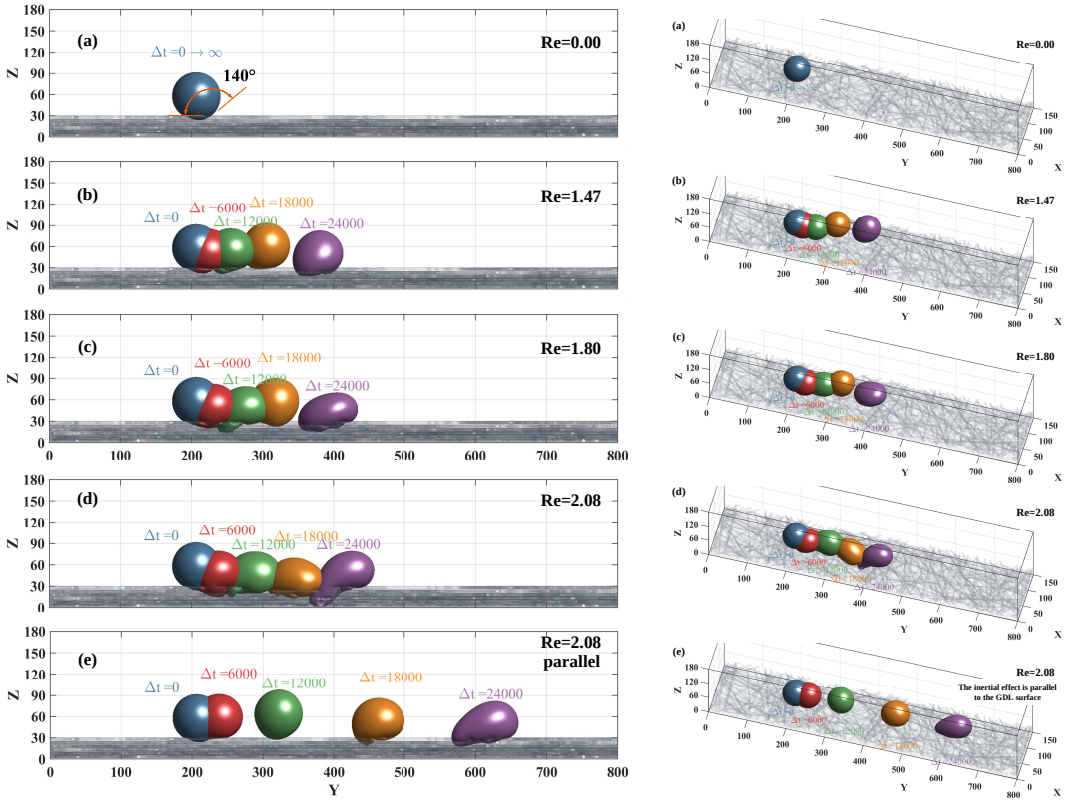

Figure 6: The front-view (left) and axis-view (right) snapshots of the droplet transport process on the GDL surface with various inertial effects.

It is obviously that the liquid droplet penetrating into the GDL can block the pore and limit the reactants transport. In order to characterize the phenomenon further, the quantitative analysis of droplet transport is performed. Figure 7 shows the time evolution of positions of the center of mass ((a)X_c, (b)Y_c, (c)Z_c) of the liquid droplet on the GDL surface. And the time-averaged normalized positions are also calculated and illustrated in Fig. 7(d). The positions are normalized by the stable positions X_s, Y_s, Z_s. As it can be seen from Figs. 7(a) and (d), the normalized X_c position for the case $Re = 1.47$ gradually enters the channel wall area (red area) while the other cases fluctuate around the initial stable position X_s. A probable explanation is that the resistance of GDL fiber is easier to overcome under the condition of higher inertia. With the increase of inertia applied

on the droplet, it is reasonable that the normalized Y_c position grows faster, as shown in Figs. 7(b) and (d). However, the time-averaged normalized Y_c position in the case with parallel inertial effect is much higher than the case with 45° inertial effect for the same Re ($Re = 2.08$). According to Figs. 7(c) and (d), as Re and time increases, the Z_c position decreases. Nevertheless the time-averaged normalized Z_c position stays at 1.0 almost the same for the case with parallel inertial effect and $Re = 1.47$. This is due to the obstruction of carbon fiber on the real GDL surface, which makes the liquid droplets fluctuate up and down. In addition, it can be seen that the center of mass Z_c position is all above the GDL surface.

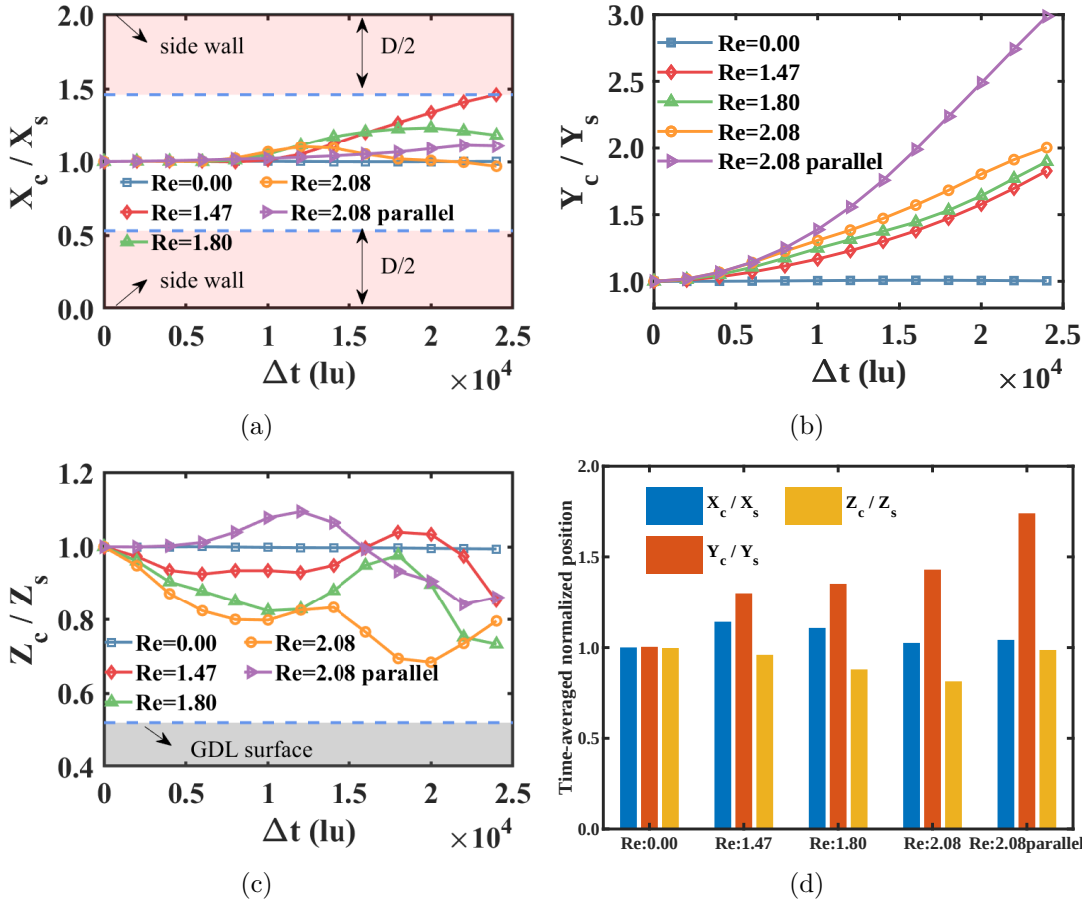

Figure 7: Time evolution of the center of mass position of the liquid droplet with various inertial effects ((a)X_c, (b)Y_c, (c)Z_c) and (d)time-averaged position. The positions are respectively normalized by the stable positions X_s, Y_s, Z_s.

The droplet penetration depth in GDL (normalized by the GDL thickness) and the droplet invasion fraction (the ratio of droplet volume in the GDL to the total volume of droplet) with various inertial effects are calculated and graphed in Fig. 8(a) and (b), respectively. The average porosity in the 1^{st} layer of GDL is 0.87, which means the pores in this layer are relatively large. Thus, the bottom of the static droplet is around the bottom of 1^{st} layer and lower than the GDL surface. For the case with lower $Re = 1.47$ and parallel inertial effect, the droplet penetration depth in GDL and the droplet invasion fraction remain almost around the base case ($Re = 0.00$). When Re increases to $Re = 1.80$, the droplet penetration depth achieves the 4^{th} layer of GDL. Because of microstructure of GDL, the droplet is drained from GDL. And then the bottom of droplet achieves the 4^{th} layer again at a later time. For the case $Re = 2.08$, the droplet firstly penetrates into the 4^{th} layer of GDL and then reaches the 6^{th} layer of GDL (GDL bottom in this study). In addition, the droplet invasion fraction changes accordingly, as shown in Fig. 8(b). The droplet invasion fraction in GDL is up to 30%. Hence, it can be described that the inertial effects toward the GDL surface cause the droplets to enter the GDL interior, and the blocking of fibrous structures of GDL make the droplet penetration depth in GDL and the droplet invasion fraction fluctuate up and down.

3.2. Effects of contact angle

The wettability of GDL exerts a vital role on the water drainage in the GDL and gas channel. In general, the more hydrophobic, the better the drainage [51]. The contact angle (CA) of the GDL is set to be 135°, 140°, and 145° to study the effects of contact angle on the liquid droplet transport on the GDL surface. The inertial effect is kept at $Re = 2.08$ and the droplet volume is the same with each other. After a same initial time t_0, the center of mass positions of droplets are gradually stable and almost the same, which are given in Table 1.

The time evolution of the center of mass position of the liquid droplet with various contact

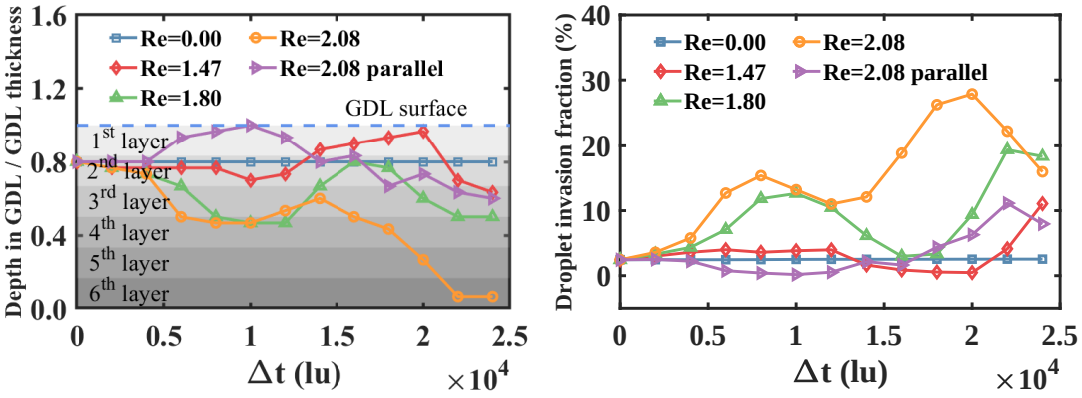

(a) (b)

Figure 8: Roles of various inertial effects on (a) the droplet penetration depth in GDL (normalized by the GDL thickness) and (b) the droplet invasion fraction (the ratio of droplet volume in the GDL to the total volume of droplet).

Table 1: The center of mass positions of the droplets on the GDL with various contact angles.

Contact angle	X_s	Y_s	Z_s
135°	72.71	206.77	57.37
140°	72.70	206.80	57.78
145°	74.71	207.53	60.08

angles and time-averaged positions is calculated and drawn in Fig. 9(a)-(d), respectively. The positions are respectively normalized by their own stable positions X_s, Y_s, Z_s. The X_c position is slightly affected by the GDL wettability and none of them reaches the channel wall (Fig. 9(a) and (c)). From the results of Y_c positions in Fig. 9(b) and (d), it can be seen that the droplet moves quickly as the contact angle increases because of low adhesion between droplet and GDL surface. This agrees well with the results of the liquid water droplet on the smooth GDL surface with different contact angle by Hao and Cheng [33]. As shown from Fig. 9(c) and (d), the Z_c position is higher when contact angle increases. Note that the case with $CA = 145°$ significantly increased after time is greater than 18000 lu.

Figure 10 shows the snapshots of droplet transport on the GDL surface with various contact angles at the time $\Delta t = 22000$. The shape of liquid droplets vary with different contact angle of GDL. It can be seen that the cases with $CA = 135°$ and $CA = 140°$ both

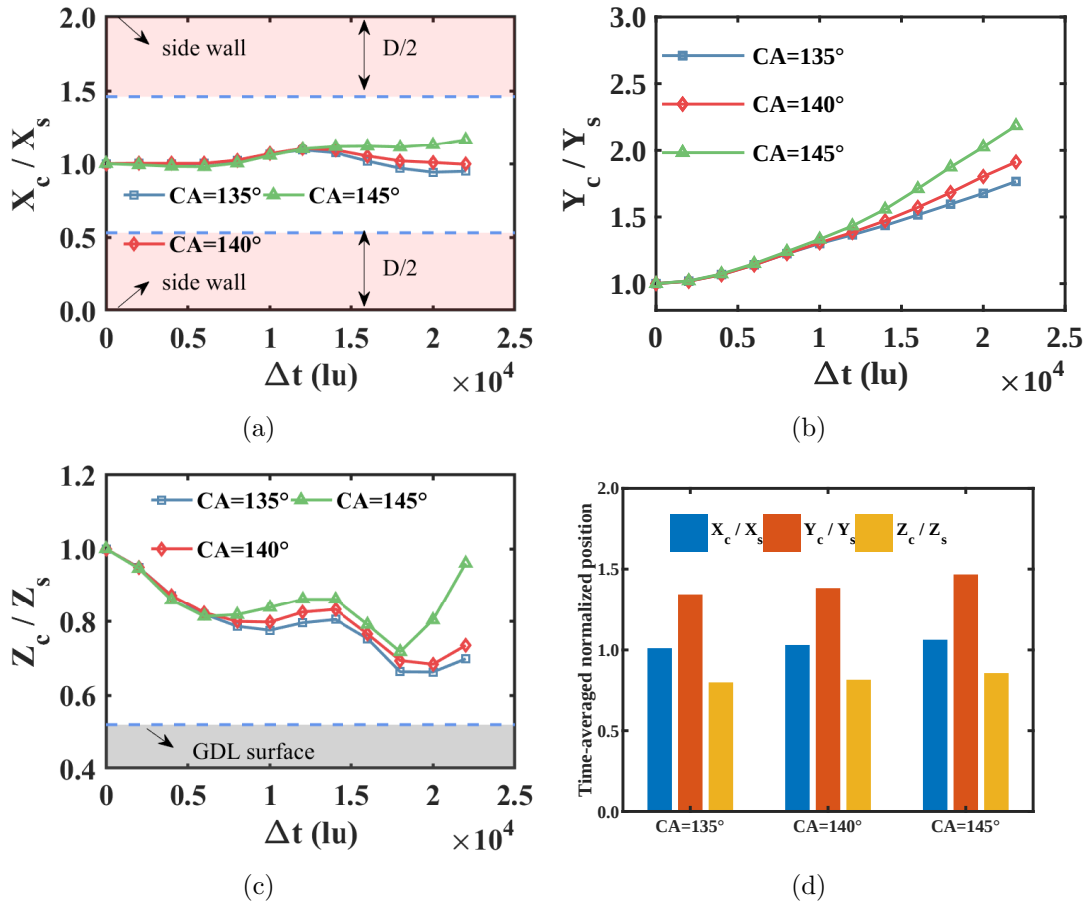

Figure 9: Time evolution of the center of mass position of the liquid droplet with various contact angles ((a)X_c, (b)Y_c, (c)Z_c) and (d)time-averaged position. The positions are respectively normalized by the stable positions X_s, Y_s, Z_s.

reach the bottom of GDL (see Fig. 10(a) and (b)). And the volume of droplet inside the GDL with $CA = 140°$ is less than that wit $CA = 135°$. However, the droplet in the case with $CA = 145°$ almost entirely outside of the GDL (see Fig. 10(c)), which is also seen from the Z_c position in Fig. 9(c).

The droplet penetration depth in GDL and the droplet invasion fraction with various contact angles are illustrated in Fig. 11. From the figures, both the cases with $CA = 135°$ and $CA = 140°$ reach the 6^{th} layer of GDL while the case with $CA = 145°$ can only reach the 3^{th} layer of GDL. This result is consistent with Eq. 16 in the section of Critical force formulation, which shows that the critical force increases when the contact angle increases.

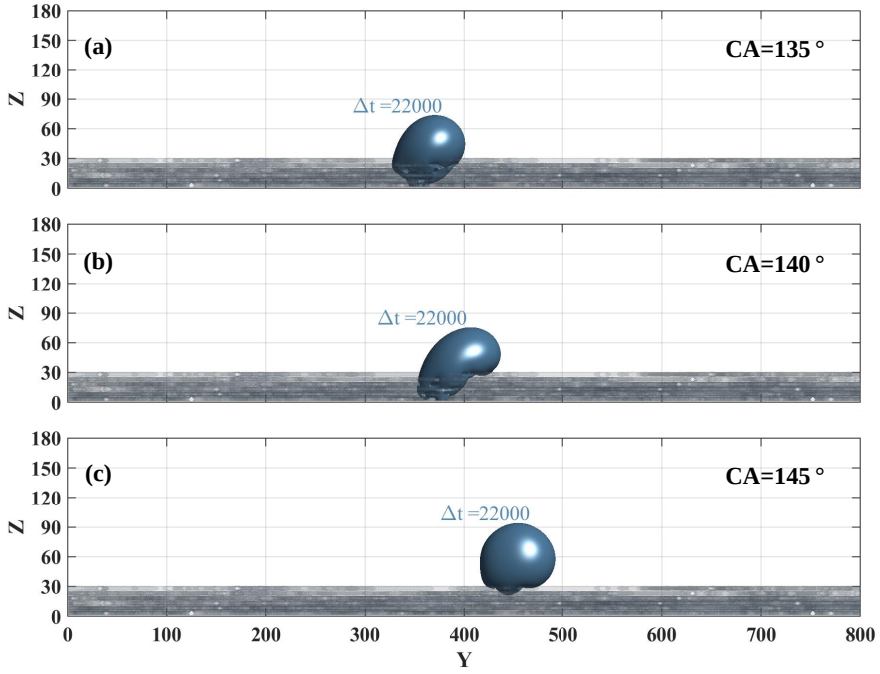

Figure 10: The front-view snapshots of the droplet transport on the GDL at time $\Delta t = 22000$ with various contact angles: (a)$CA = 135°$, (b)$CA = 140°$, and (c)$CA = 145°$.

Therefore, for the same inertial force, the droplet invasion fraction decreases as the increase of contact angle (see Fig. 11(b)). From the above observations, a possible cause for the droplet to move faster with larger contact angle might be attributed to the smaller embedded part of droplet inside the GDL and smaller contact area between the droplet and GDL surface.

4. Conclusion

In this study, the simulation of the dynamic behavior of liquid droplets on the reconstructed real GDL surface with the inertial effect is conducted by the means of an improved pseudopotential multiphase LB model, which can realize thermodynamic consistency and tunable surface tension. The microstructure of the GDL (Toray-090) including carbon fibers and PTFE is reconstructed by a stochastic and mixed-wettability model. The critical force formulation for the Cassie-Wenzel transition of a droplet on GDL surface is derived. The

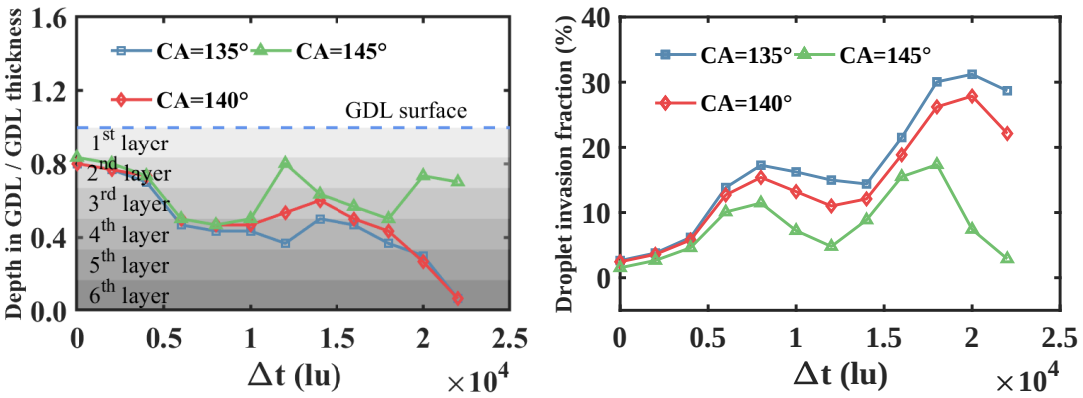

Figure 11: Effects of various contact angles on (a) the droplet penetration depth in GDL (normalized by the GDL thickness) and (b) the droplet invasion fraction (the ratio of droplet volume in the GDL to the total volume of droplet).

roles of inertial effects and the effects of contact angles on the liquid droplet transport process on a reconstructed real GDL surface with a 3D flow channel are investigated. The time evolution liquid droplet movement on the GDL surface is captured by the ULBM simulation. The main conclusions of the study are:

1) The normalized X_c position for the case $Re = 1.47$ gradually enters the channel wall area while those of the other cases fluctuate around the initial stable position. With the increase of inertia applied on the droplet, the normalized Y_c position grows faster and the Z_c position decreases.

2) The droplet is pushed back into the GDL by inertial effect. And the higher the inertial effect is, the more deeply the liquid droplet penetrates into the GDL.

3) With the increase of inertial effect or the decrease of contact angle of GDL, both the droplet penetration depth in GDL and the droplet invasion fraction increase. The droplet invasion fraction in GDL is up to 30%.

4) The X_c position is slightly affected by the GDL wettability and none of them reach the channel wall. And the droplet moves quickly and the Z_c position is higher when the contact angle increases.

The liquid droplet re-penetrating into the GDL can block the pore and limit the reactants transport under the condition of 3D flow channel. In order to better enhance the performance of 3D flow channel, further studies on the effects of droplet radius, the angle of the inertial force, and the collaborative optimization of GDL structure and 3D flow channel are needed in the future.

Acknowledgement

This research is supported by the the National Key R&D Program of China (Grant No. 2020YFB0106604). Supercomputing time on ARCHER2 is provided by the "UK Consortium on Mesoscale Engineering Sciences (UKCOMES)" under the UK Engineering and Physical Sciences Research Council Grant No. EP/R029598/1.

References

[1] K. Jiao, X. Li, Water transport in polymer electrolyte membrane fuel cells, Progress in energy and combustion Science 37 (2011) 221–291.

[2] S. J. Peighambardoust, S. Rowshanzamir, M. Amjadi, Review of the proton exchange membranes for fuel cell applications, International journal of hydrogen energy 35 (2010) 9349–9384.

[3] Y. Wang, D. F. R. Diaz, K. S. Chen, Z. Wang, X. C. Adroher, Materials, technological status, and fundamentals of pem fuel cells–a review, Materials Today (2019).

[4] J. Zhao, X. Li, A review of polymer electrolyte membrane fuel cell durability for vehicular applications: Degradation modes and experimental techniques, Energy Conversion and Management 199 (2019) 112022.

[5] S. G. Kandlikar, E. J. See, M. Koz, P. Gopalan, R. Banerjee, Two-phase flow in gdl and reactant channels of a proton exchange membrane fuel cell, international journal of hydrogen energy 39 (2014) 6620–6636.

[6] J. Cho, T. Neville, P. Trogadas, J. Bailey, P. Shearing, D. Brett, M.-O. Coppens, Capillaries for water management in polymer electrolyte membrane fuel cells, international journal of hydrogen energy 43 (2018) 21949–21958.

[7] P. Moçotéguy, B. Ludwig, D. Beretta, T. Pedersen, Study of the impact of water management on the performance of pemfc commercial stacks by impedance spectroscopy, International Journal of Hydrogen Energy 45 (2020) 16724–16737.

[8] X. Ma, X. Zhang, J. Yang, W. Zhuge, S. Shuai, Impact of gas diffusion layer spatial variation properties on water management and performance of pem fuel cells, Energy Conversion and Management 227 (2021) 113579.

[9] R. Omrani, B. Shabani, Gas diffusion layer modifications and treatments for improving the performance of proton exchange membrane fuel cells and electrolysers: a review, international journal of hydrogen energy 42 (2017) 28515–28536.

[10] A. Bazylak, Liquid water visualization in pem fuel cells: A review, International journal of hydrogen energy 34 (2009) 3845–3857.

[11] Z. Lu, C. Rath, G. Zhang, S. G. Kandlikar, Water management studies in pem fuel cells, part iv: Effects of channel surface wettability, geometry and orientation on the two-phase flow in parallel gas channels, International Journal of Hydrogen Energy 36 (2011) 9864–9875.

[12] E. Kumbur, K. Sharp, M. Mench, Liquid droplet behavior and instability in a polymer electrolyte fuel cell flow channel, Journal of Power Sources 161 (2006) 333–345.

[13] A. Theodorakakos, T. Ous, M. Gavaises, J. Nouri, N. Nikolopoulos, H. Yanagihara, Dynamics of water droplets detached from porous surfaces of relevance to pem fuel cells, Journal of colloid and interface science 300 (2006) 673–687.

[14] J. Z. Fishman, H. Leung, A. Bazylak, Droplet pinning by pem fuel cell gdl surfaces, International journal of hydrogen energy 35 (2010) 9144–9150.

[15] T. Wu, N. Djilali, Experimental investigation of water droplet emergence in a model polymer electrolyte membrane fuel cell microchannel, Journal of Power Sources 208 (2012) 248–256.

[16] P. Rahimian, L. Battrell, R. Anderson, N. Zhu, E. Johnson, L. Zhang, Investigation of time dependent water droplet dynamics on porous fuel cell material via synchrotron based x-ray imaging technique, Experimental Thermal and Fluid Science 97 (2018) 237–245.

[17] A. Iranzo, A. Salva, P. Boillat, J. Biesdorf, E. Tapia, F. Rosa, Water build-up and evolution during the start-up of a pemfc: Visualization by means of neutron imaging, International Journal of Hydrogen Energy 42 (2017) 13839–13849.

[18] X. Wang, W. Wang, Z. Qu, G. Ren, H. Wang, Surface roughness dominated wettability of carbon fiber in gas diffusion layer materials revealed by molecular dynamics simulations, International Journal of

Hydrogen Energy (2021).

[19] X. Zhu, P. Sui, N. Djilali, Dynamic behaviour of liquid water emerging from a gdl pore into a pemfc gas flow channel, Journal of Power Sources 172 (2007) 287–295.

[20] L. Chen, Y.-L. He, W.-Q. Tao, Effects of surface microstructures of gas diffusion layer on water droplet dynamic behaviors in a micro gas channel of proton exchange membrane fuel cells, International journal of heat and mass transfer 60 (2013) 252–262.

[21] M. Ashrafi, M. Shams, Effects of heterogeneous surface of gas diffusion layers on droplet transport in microchannels of pem fuel cells, International Journal of Hydrogen Energy 41 (2016) 1974–1989.

[22] I. S. Anyanwu, Z. Niu, D. Jiao, A.-U.-H. Najmi, Z. Liu, K. Jiao, et al., Liquid water transport behavior at gdl-channel interface of a wave-like channel, Energies 13 (2020) 2726.

[23] Y. Bao, Y. Gan, Roughness effects of gas diffusion layers on droplet dynamics in pemfc flow channels, International Journal of Hydrogen Energy 45 (2020) 17869–17881.

[24] R. Chen, Y. Qin, S. Ma, Q. Du, Numerical simulation of liquid water emerging and transport in the flow channel of pemfc using the volume of fluid method, International Journal of Hydrogen Energy 45 (2020) 29861–29873.

[25] D. K. Dang, B. Zhou, Liquid water transport in pemfc cathode with symmetrical biomimetic flow field design based on murray's law, International Journal of Hydrogen Energy 46 (2021) 21059–21074.

[26] Y. Cai, T. Yang, P.-C. Sui, J. Xiao, A numerical investigation on the effects of water inlet location and channel surface properties on water transport in pemfc cathode channels, International journal of hydrogen energy 41 (2016) 16220–16229.

[27] Q. Li, K. H. Luo, Q. Kang, Y. He, Q. Chen, Q. Liu, Lattice boltzmann methods for multiphase flow and phase-change heat transfer, Progress in Energy and Combustion Science 52 (2016) 62–105.

[28] Q. Li, Q. Kang, M. M. Francois, Y. He, K. H. Luo, Lattice boltzmann modeling of boiling heat transfer: The boiling curve and the effects of wettability, International Journal of Heat and Mass Transfer 85 (2015) 787–796.

[29] L. Fei, K. H. Luo, C. Lin, Q. Li, Modeling incompressible thermal flows using a central-moments-based lattice boltzmann method, International Journal of Heat and Mass Transfer 120 (2018) 624–634.

[30] L. Fei, A. Scagliarini, A. Montessori, M. Lauricella, S. Succi, K. H. Luo, Mesoscopic model for soft flowing systems with tunable viscosity ratio, Physical Review Fluids 3 (2018) 104304.

[31] L. Fei, J. Yang, Y. Chen, H. Mo, K. H. Luo, Mesoscopic simulation of three-dimensional pool boiling based on a phase-change cascaded lattice boltzmann method, Physics of Fluids 32 (2020) 103312.

[32] G. Molaeimanesh, H. S. Googarchin, A. Q. Moqaddam, Lattice boltzmann simulation of proton exchange membrane fuel cells–a review on opportunities and challenges, International Journal of Hydrogen Energy 41 (2016) 22221–22245.

[33] L. Hao, P. Cheng, Lattice boltzmann simulations of liquid droplet dynamic behavior on a hydrophobic surface of a gas flow channel, Journal of power sources 190 (2009) 435–446.

[34] M. E. A. B. Amara, S. B. Nasrallah, Numerical simulation of droplet dynamics in a proton exchange membrane (pemfc) fuel cell micro-channel, International journal of hydrogen energy 40 (2015) 1333–1342.

[35] A. Xu, T. Zhao, L. An, L. Shi, A three-dimensional pseudo-potential-based lattice boltzmann model for multiphase flows with large density ratio and variable surface tension, International Journal of Heat and Fluid Flow 56 (2015) 261–271.

[36] J. Yang, X. Ma, L. Fei, X. Zhang, K. H. Luo, S. Shuai, Effects of hysteresis window on contact angle hysteresis behaviour at large bond number, Journal of Colloid and Interface Science 566 (2020) 327–337.

[37] Y. Hou, H. Deng, N. Zamel, Q. Du, K. Jiao, 3d lattice boltzmann modeling of droplet motion in pem fuel cell channel with realistic gdl microstructure and fluid properties, International Journal of Hydrogen Energy (2020).

[38] J.-K. Kuo, et al., A novel nylon-6–s316l fiber compound material for injection molded pem fuel cell bipolar plates, Journal of Power Sources 162 (2006) 207–214.

[39] J.-K. Kuo, et al., Evaluating the enhanced performance of a novel wave-like form gas flow channel in the pemfc using the field synergy principle, Journal of Power Sources 162 (2006) 1122–1129.

[40] Y. Wang, Porous-media flow fields for polymer electrolyte fuel cells i. low humidity operation, Journal of The Electrochemical Society 156 (2009) B1124–B1133.

[41] Y. Wang, Porous-media flow fields for polymer electrolyte fuel cells ii. analysis of channel two-phase flow, Journal of The Electrochemical Society 156 (2009) B1134–B1141.

[42] S.-W. Perng, H.-W. Wu, R.-H. Wang, Effect of modified flow field on non-isothermal transport characteristics and cell performance of a pemfc, Energy conversion and management 80 (2014) 87–96.

[43] W. Li, Q. Zhang, C. Wang, X. Yan, S. Shen, G. Xia, F. Zhu, J. Zhang, Experimental and numerical analysis of a three-dimensional flow field for pemfcs, Applied Energy 195 (2017) 278–288.

[44] T. Yoshida, K. Kojima, Toyota mirai fuel cell vehicle and progress toward a future hydrogen society, Electrochemical Society Interface 24 (2015) 45.

[45] J. Kim, G. Luo, C.-Y. Wang, Modeling two-phase flow in three-dimensional complex flow-fields of

proton exchange membrane fuel cells, Journal of Power Sources 365 (2017) 419–429.

[46] Y.-H. Qian, D. d'Humières, P. Lallemand, Lattice bgk models for navier-stokes equation, EPL (Europhysics Letters) 17 (1992) 479.

[47] D. d'Humieres, Multiple–relaxation–time lattice boltzmann models in three dimensions, Philosophical Transactions of the Royal Society of London. Series A: Mathematical, Physical and Engineering Sciences 360 (2002) 437–451.

[48] L. Fei, K. H. Luo, Q. Li, Three-dimensional cascaded lattice boltzmann method: Improved implementation and consistent forcing scheme, Physical Review E 97 (2018) 053309.

[49] L. Fei, J. Du, K. H. Luo, S. Succi, M. Lauricella, A. Montessori, Q. Wang, Modeling realistic multiphase flows using a non-orthogonal multiple-relaxation-time lattice boltzmann method, Physics of Fluids 31 (2019) 042105.

[50] K. H. Luo, L. Fei, G. Wang, A unified lattice boltzmann model and application to multiphase flows, Philosophical Transactions of The Royal Society A-Mathematical Physical and Engineering Sciences (2021).

[51] J. Yang, L. Fei, X. Zhang, X. Ma, K. H. Luo, S. Shuai, Improved pseudopotential lattice boltzmann model for liquid water transport inside gas diffusion layers, International journal of hydrogen energy 46 (2021) 15938–15950.

[52] J. Yang, K. H. Luo, X. Ma, Y. Li, S. Shuai, Effects of perforation shapes on water transport in pemfc gas diffusion layers, SAE International Journal of Advances and Current Practices in Mobility 1 (2019) 808–814. 2019-01-0380.

[53] J. Yang, X. Ma, T. Lei, K. H. Luo, S. Shuai, Numerical simulations for optimizing the liquid water transport in the gas diffusion layer and gas channels of a pemfc, Journal of Tsinghua University(Science and Technology) 59 (2019) 580 – 586.

[54] L. Chen, Q. Kang, Y. Mu, Y.-L. He, W.-Q. Tao, A critical review of the pseudopotential multiphase lattice boltzmann model: Methods and applications, International Journal of Heat and Mass Transfer 76 (2014) 210–236.

[55] X. Shan, H. Chen, Lattice boltzmann model for simulating flows with multiple phases and components, Physical Review E 47 (1993) 1815.

[56] X. Shan, H. Chen, Simulation of nonideal gases and liquid-gas phase transitions by the lattice boltzmann equation, Physical Review E 49 (1994) 2941.

[57] P. Yuan, L. Schaefer, Equations of state in a lattice boltzmann model, Physics of Fluids 18 (2006)

042101.

[58] Q. Li, K. H. Luo, Q. Kang, Q. Chen, Contact angles in the pseudopotential lattice boltzmann modeling of wetting, Physical Review E 90 (2014) 053301.

[59] R. N. Wenzel, Surface roughness and contact angle., The Journal of Physical Chemistry 53 (1949) 1466–1467.

[60] A. Cassie, S. Baxter, Wettability of porous surfaces, Transactions of the Faraday society 40 (1944) 546–551.

[61] Q.-S. Zheng, Y. Yu, Z.-H. Zhao, Effects of hydraulic pressure on the stability and transition of wetting modes of superhydrophobic surfaces, Langmuir 21 (2005) 12207–12212.

[62] Z. Fishman, A. Bazylak, Heterogeneous through-plane porosity distributions for treated pemfc gdls i. ptfe effect, Journal of The Electrochemical Society 158 (2011) B841.